Research Article

Journal of
Environmental
Nanotechnology

Synthesis of Ag-decorated TiO_2 Nanoparticles for Ammonia Gas Sensor Application

T. Kalaivani[1], P. Anil Kumar[2], Samridhi[3], K. Balachandran[4]*
[1]Department of Chemistry, Research & Development Centre, Bharathiar University, Coimbatore, TN, India
[2]Department of Chemistry, KPR Institute of Engineering and Technology, Coimbatore, TN, India
[3]Department of Physics, Banasthali Vidyapith, Banasthali, RJ, India
[4]Department of Chemistry, Vivekanandha College of Engineering for Women, Namakkal, TN, India
Received: 05.07.2021 Accepted: 17.08.2021 Published: 30-09-2021
*balachandran@vcew.ac.in

ABSTRACT

In this research, nanometer-sized clusters of TiO_2 have been successfully synthesized through the Sol-gel method. Further, different concentrations of Ag were deposited on TiO_2. After the successful deposition of Ag on TiO_2, the gas sensing performance of the sample has been studied at different exposure of NH_3 (ammonia) gas. Analysis has been done via XRD to evaluate the grain size of the nanoparticles and calculated as 18 nm for TiO_2 and 12 nm for 5 % Ag-doped TiO_2. EDS has been conducted, ensuring that Ag has been successfully decorated on the superficial of TiO_2. The formation of nano-size particles has been confirmed by TEM analysis. FTIR analysis confirmed the existence of TiO_2 and Ag. The surface state emission of TiO_2: Ag nanoparticles can be seen in the PL spectrum at 383 nm, 450 nm and 465 nm. As the exposure of NH_3 gas increases from 50 to 250 ppm, the impedance range displayed a decrease in semicircle radius, which was then marginally increased. The variance in resistance also contributed to the gas sensing properties due to grain boundaries, in accordance with impedance spectroscopy review.

Keywords: Gas Sensor; Impedance; Titanium dioxide (TiO_2).

1. INTRODUCTION

Since the 20th century, the increase in vehicle and industrial emissions has led to increased atmospheric pollutants. These pollutants have worsened air quality. Inhalation of such toxic gases like CO, H_2S, NO_2 and NH_3 leads to instantaneous and adverse effects on human health, of which ammonia (NH_3) is the one causing the most severe environmental problems. The excess of ammonia in the environment causes nutrient imbalances in plant species and in aquatic ecosystems (Pinder *et al.* 2008). In recent years, research is focused on developing intelligent monitoring systems to supervise air quality control heating, ventilation and air conditioning to ensure the safety of our environment. The development of NH_3 gas sensors using nanomaterial has earned a lot of interest due to an array of applications in medical diagnostics (de la Hoz *et al.* 1996; Ament *et al.* 1999), automotive exhaust detection (Tang *et al.* 2014; Wang *et al.* 2015), industrial emission monitoring (Yu'e *et al.* 2000) and environmental monitoring (Erisman *et al.* 2001). Metal oxide gas sensors (Izu *et al.* 2011), organic gas sensors (Lehner *et al.* 2014), carbon-based gas sensors (Borini *et al.* 2013), electrochemical gas sensors (Miura *et al.* 2003), solid electrolyte-based gas sensors (Weppner *et al.* 1987) are just a few of the gas sensors developed so far. Among the various types of gas sensors, the resistance-based metal oxide gas sensor has gained popularity in recent years due to its low cost, ease of fabrication and increased sensitivity (Kalaivani *et al.* 2018b).

In 1962, Seiyama was the first to discover gas sensitivity on metal oxides and Taguchi brought metal oxide semiconductor-based gas sensors to the marketplace. Resistive-type gas sensors are popular for their easy availability at low cost and high durability but with limited sensitivity and selectivity. Countless efforts have been made to enhance the sensing properties by controlling the shape and size of the metal oxide (Gurlo *et al.* 2011), by adding catalysts to the sensing layer (Shi *et al.* 2013).

To enhance these properties, wide gap semiconductors have been extensively used as sensing material such as n-type (ZnO, SnO_2, TiO_2) and p-type (NiO, CuO, Co_3O_4) metal oxides (Sharma *et al.* 2019b). However, n-type semiconductors are utilized more in work because the mobility of charge carriers is higher than that of p-types. The carrier concentration of such materials is determined by oxygen non-stoichiometry and by aliovalent cations (Kılıç *et al.* 2002; Sharma *et al.* 2019a). Among different materials, TiO_2 has attracted considerable attention because of its tolerance in harsh environments, high stability, and eco-friendly properties, which make the sensor most stable and potential. TiO_2 is an n-type wide bandgap semiconductor, with 3.1 eV to 3.3 eV for rutile and anatase phase structure,

https://dx.doi.org/10.13074/jent.2021.09.213443

respectively. Both phases of TiO_2 show promising results in gas sensor applications (Kalaivani *et al.* 2018a), such as UV detector (Hossein-Babaei *et al.* 2012), solar cell fabrication (McFarland *et al.* 2003) and photocatalysis (Balachandran *et al.* 2018; 2021). The NPs of noble materials (like Ag, Pd, Au, Pt, Rh) improve the thermal stability of the film and enhance device properties. Ag-doped TiO_2 nanoparticles show many striking characteristics; it is cheaper than other noble materials and has higher oxygen adsorption reactivity and higher efficiency. In Ag, cationic mobility is high, therefore it can be used as a resistive switching device.

In this research, a main focus is emphasized on the synthesis of Ag-decorated TiO_2 NPs by Sol-gel method. This research aims to endorse the gas sensing performance towards NH_3. Various characterization techniques like XRD, SEM, TEM, FT-IR and PL analyses have been used to explore the purpose of using the Silver-doped TiO_2 nanoparticles to be used in gas sensors. The diffusion of noble material like silver into the TiO_2 layer plays an important role in investigating sensor sensitivity.

2. EXPERIMENTAL PROCEDURE

2.1 Preparation of TiO_2 NPs

The TiO_2 NPs have been synthesized by means of titanium tetra isopropoxide (TTIP) as a precursor, ethanol as a solvent, and hydrochloric acid (HCl) as a peptizing agent to make TiO_2 nanoparticles. To prepare TiO_2 nanoparticles, 10 ml of HCl was mixed with 50 ml ethanol and stirred for a couple of minutes. 100 ml TTIP was added to this mixture and the stirring was done continuously for an hour at room temperature. 500 ml of DI water was then added and the temperature was raised to 50 °C and the solution has been continued to be stirred for 5 hours before it turned into colorless gel. The high viscous gel was dried to a fine powder at room temperature. In a hot air oven, the powder was heated at 120 °C for an hour. Finally, the colorless powder has been calcined for 2 hours at 400 °C. The synthesis steps have been depicted through a flow chart, as illustrated in fig.1.

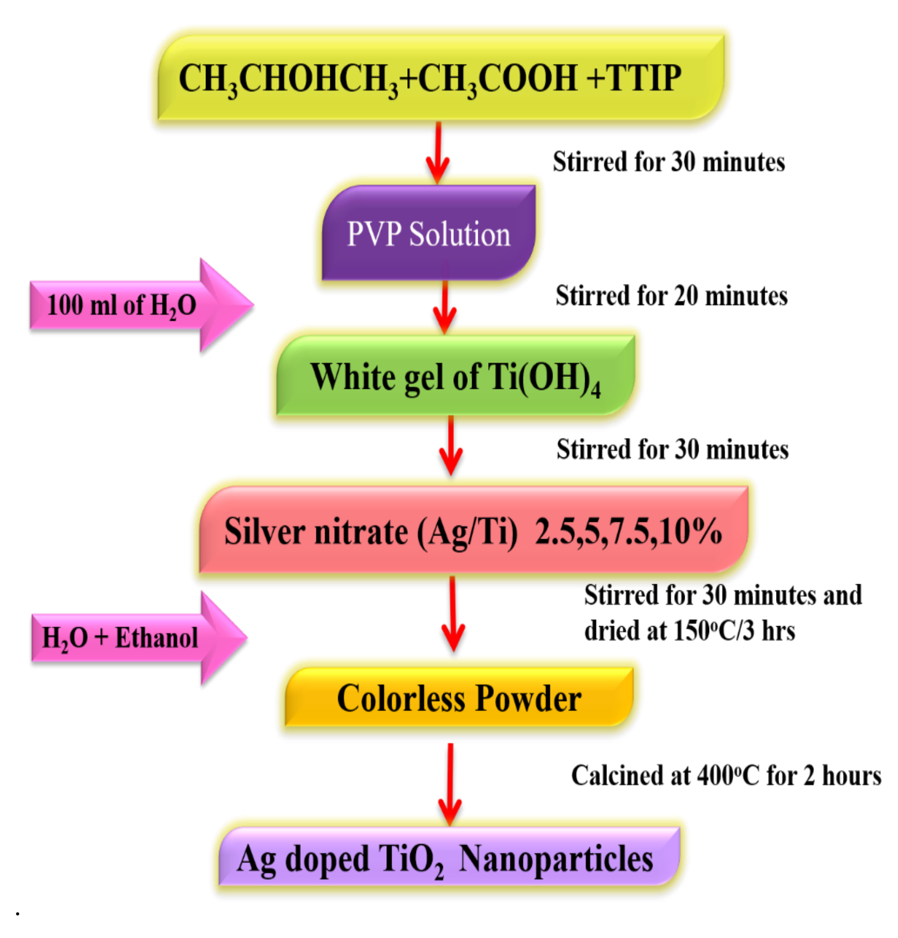

Fig. 1: Flowchart of Synthesis of TiO_2: Ag NPs

2.2 Synthesis of Ag-doped TiO_2 NPs

The TiO_2 solution has been made using the method discussed in the former section. $AgNO_3$ solutions in different concentrations (2.5 % to 10 %) were added to form Ag-TiO_2 composites. Different concentration of $AgNO_3$ solution has been taken into account with an increment of 2.5 % ranging from 2.5 % to 10 %. The solution's overall concentrations were held at 0.1 mol/liter. After adding the Ag ions to the TiO_2 solution, stirring was continued for 3 hours and the temperature was maintained at 80 ˚C. The fine precipitate has been washed away with DI water and dried at 120 ˚C for an hour. The powder so obtained was calcined for 2 hours at 400 ˚C. Synthesis steps of anatase phase TiO_2 nanoparticles are illustrated below in Fig. 2.

2.3 Characterization

To investigate the gas sensing properties, the sample has been characterized by using BrukerD8 ADVANCE diffractometer meter with Cu-K (**λ** = 0.15406 nm) radiation at an operating voltage of 30 kV at 30 mA supply. Scherrer's formula analyzed the XRD plots to investigate numerous parameters like d-spacing, lattice constant, volume, and crystallite size. Surface morphological studies of the sample have been analyzed by field emission scanning electron microscope (FESEM) of TiO_2 NPs and Ag-TiO_2 nanocomposites (Model JSM 6390LV, JOEL, USA). A transmission electron microscope (TEM) (JEOL-TEM 2100) has been used and set at high magnification to know the precise size of NPs. The functional groups have been analyzed by FTIR spectra, for the electronic structure PL spectrum has been utilized, respectively. In the forthcoming section, a detailed analysis of various characterization techniques has been done.

3. CHARACTERIZATION TECHNIQUES

3.1 Structural and morphological characteristics

XRD has been conducted to investigate the crystal structure of TiO_2 and Ag -TiO_2 NPs. Fig. 3 illustrate the diffraction peaks for TiO_2 obtained at (101), (110), (103), (004), (112), (220), (114), (105), (211), (204), (116), (220), (301) and (206) which confirm the formation of anatase phase (Liu *et al.* 2000). The main diffraction peak at 2θ=25.3° corresponds to (101) plane, which shows the anatase phase formation (JCPDS card no.21-1272). The Ag ions were well-dispersed in the TiO_2 surface, which does not offer any diffraction in XRD, as shown in Fig. 3a to 3e.

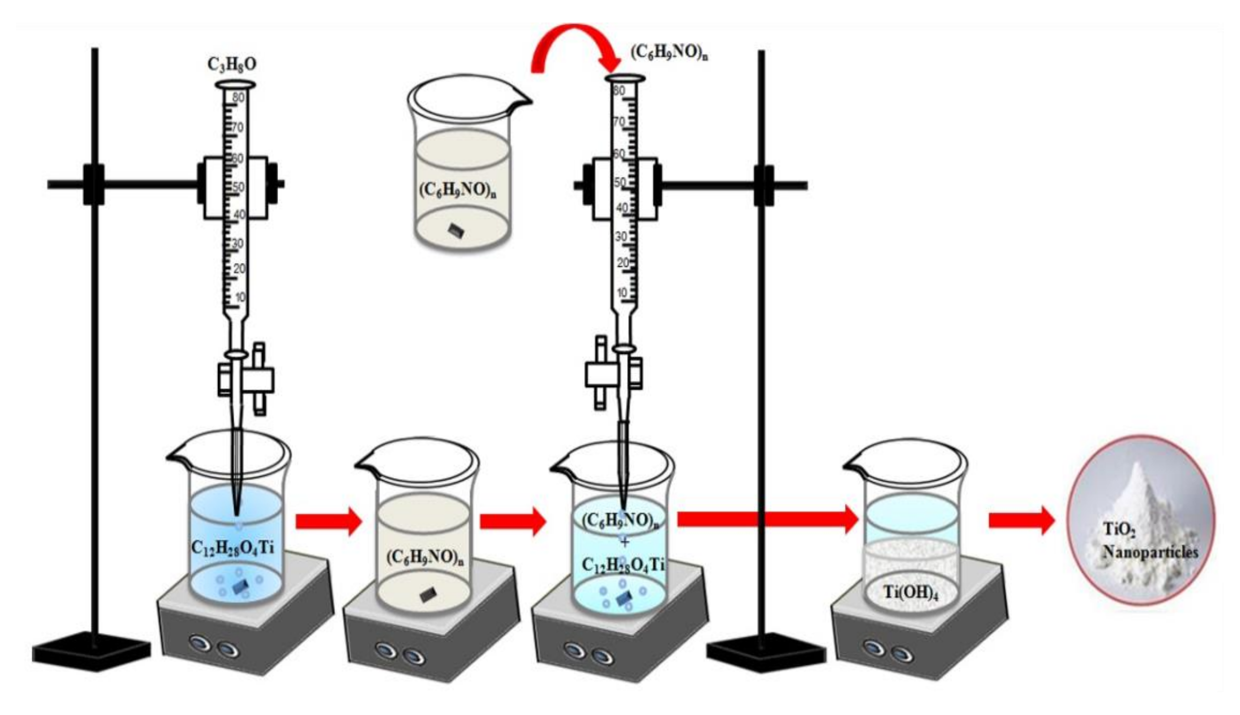

Fig. 2. Schematic of the synthesis of anatase phase TiO_2 nanoparticles

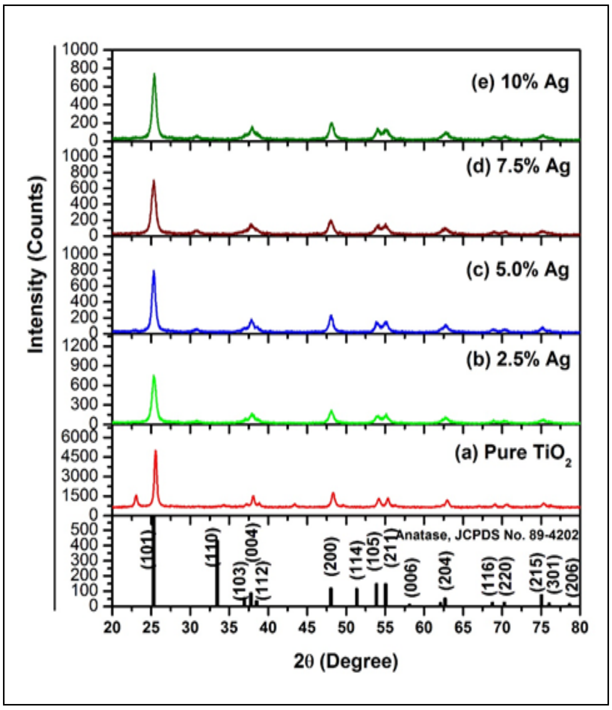

Fig. 3. XRD patterns of TiO$_2$ and Ag-doped TiO$_2$ nanocomposites

The crystal structure of anatase TiO$_2$ has not been altered after the deposition of silver. The silver dopants are simply positioned at the superficial of the crystal rather than being covalently anchored into the crystal lattice. The diffraction patterns of pure TiO$_2$ and Ag-TiO$_2$NPs had a wide line width, which ensured that particle size was small. Scherrer's equation has been used to calculate the grain size D, the full width at half maximum (FWHM) of the (101) diffraction peak.

$$D = \frac{K\lambda}{\beta\cos\theta} \qquad (1)$$

where *D* is the value of crystallite size, *λ* is the wavelength of Cu-K_α(1.54056 Å) radiation, *β* is FWHM of the corresponding diffraction peak measured in radian, *K* is Scherrer constant (0.89) and *θ* is the angle of diffraction. The calculated grain size of TiO$_2$ was notedaround~18 nm, then it was reduced by doping of Ag in TiO$_2$ and it was found to be 15 nm for 2.5 % and 12 nm for 5 % Ag-doped TiO$_2$. Then it was increased to 20 nm for 7.5 % and 10 % Ag-doped TiO$_2$. This data strongly suggests that increasing the Ag concentration increases the grain size due to the agglomeration of Ag on TiO$_2$.

3.2 FESEM and TEM analysis of TiO$_2$ and Ag TiO$_2$ NPs

scanning electron microscopy (SEM) technique has been used to investigate the grain size and it was found to be ~12 to 14 nm. Fig. 4a illustrates the SEM images of TiO$_2$ and Ag-TiO$_2$ with different magnification. The synthesized NPs shown in SEM images had irregular morphology with smooth, dense and pinhole-like grains. Further, elemental analysis of the prepared samples has been accomplished, as shown in Fig. 4 d. confirming the ratio of elements present in the sample. The EDX spectra confirm Ag, Ti, and O elements in Ag-doped TiO$_2$ nanoparticles.

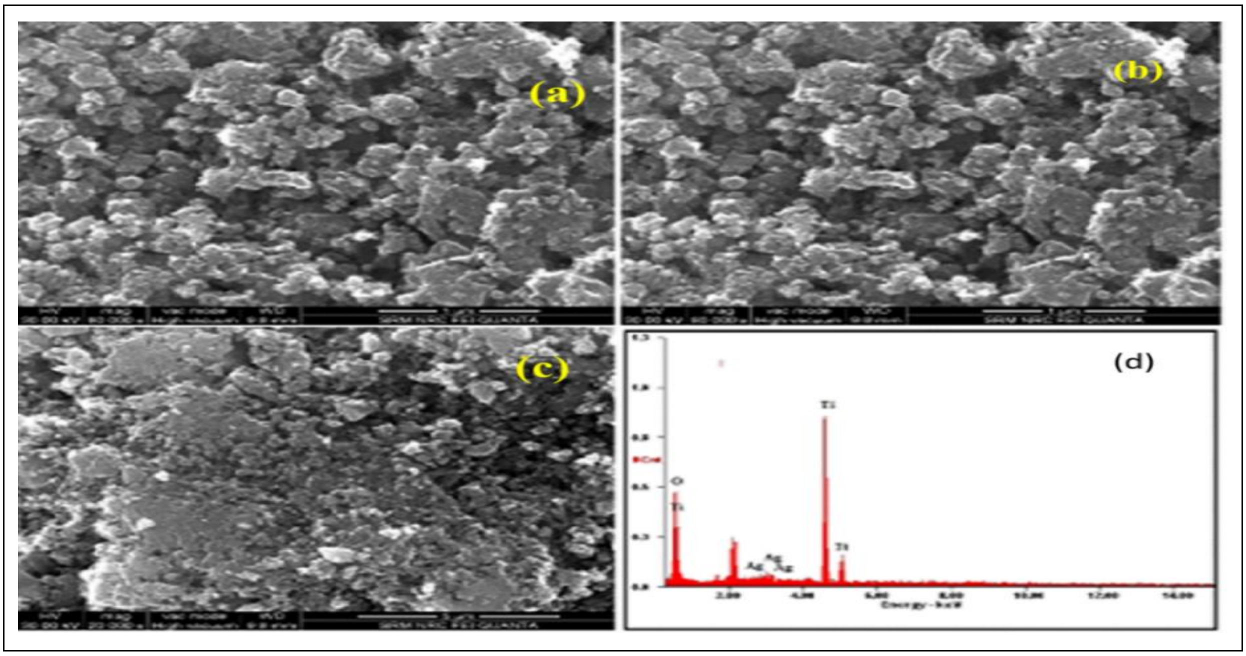

Fig. 4: (a, b, c) SEM images of TiO$_2$ and Ag-doped TiO$_2$ nano-composites (d) EDAX spectrum

Table 1. Obtained parameters from XRD pattern of d spacing corresponding to assigned rings

Doping conc.	Pos [^{O}2Th.]	d-spacing [Å]	FWHM [^{O}2Th.]	h	k	l	Lattice Constant (Å)		Crystalline size (nm)	Micro strain (ε) 10^{-4} lin^{-2}m^{-4}	Dislocation density (δ) 10^{15}lin/m^2
							a	c			
Pure TiO_2	25.557	3.486	0.427	1	0	1	3.798	9.531	19.90	18.10	2.52
	38.012	1.890	0.345	1	1	2			25.40	14.20	1.54
	48.020	1.899	0.167	2	0	0			54.50	6.63	33.63
	55.351	1.660	0.475	2	1	1			19.70	18.30	2.56
	62.963	1.476	0.546	2	0	4			17.80	20.30	3.14
	70.640	1.333	0.185	2	2	0			55.10	6.50	32.93
	75.330	1.262	0.461	2	1	5			22.70	15.90	1.93
2.5% Ag	25.363	3.509	0.639	1	0	1	3.813	9.383	13.30	27.20	5.64
	48.090	1.891	0.760	2	0	0			10.80	33.40	8.55
	53.980	1.698	0.840	2	1	1			9.30	38.80	0.11
	62.800	1.477	1.000	2	0	4			9.70	37.20	0.10
	69.060	1.346	2.280	2	2	0			4.40	81.50	0.50
	75.030	1.263	0.980	2	1	5			10.60	33.80	8.76
5% Ag	25.310	3.516	0.554	1	0	1	3.836	9.338	15.30	23.50	4.24
	48.090	1.891	0.606	2	0	0			14.90	24.10	4.45
	53.980	1.697	0.740	2	1	1			12.50	28.70	6.31
	62.800	1.479	0.930	2	0	4			10.40	34.60	9.50
	69.060	1.359	2.150	2	2	0			4.70	77.20	0.45
	75.030	1.265	0.790	2	1	5			13.20	27.30	5.70
7.5% Ag	25.304	3.517	0.683	1	0	1	3.806	9.409	12.40	29.10	6.45
	48.000	1.894	0.780	2	0	0			11.60	31.10	7.37
	54.510	1.682	1.820	2	1	1			5.10	70.50	0.38
	62.780	1.479	1.120	2	0	4			8.70	41.70	0.13
	69.850	1.345	2.210	2	2	0			4.60	79.10	0.47
	75.190	1.263	1.320	2	1	5			7.90	45.60	0.15
10% Ag	25.373	3.507	0.608	1	0	1	3.811	9.411	13.90	25.80	5.11
	48.070	1.891	0.685	2	0	0			13.20	27.20	5.68
	54.100	1.694	0.700	2	1	1			13.30	27.20	5.64
	62.840	1.478	1.060	2	0	4			9.20	39.40	0.11
	69.840	1.346	2.270	2	2	0			4.50	81.20	0.50
	75.050	1.265	1.320	2	1	5			7.90	45.60	0.15

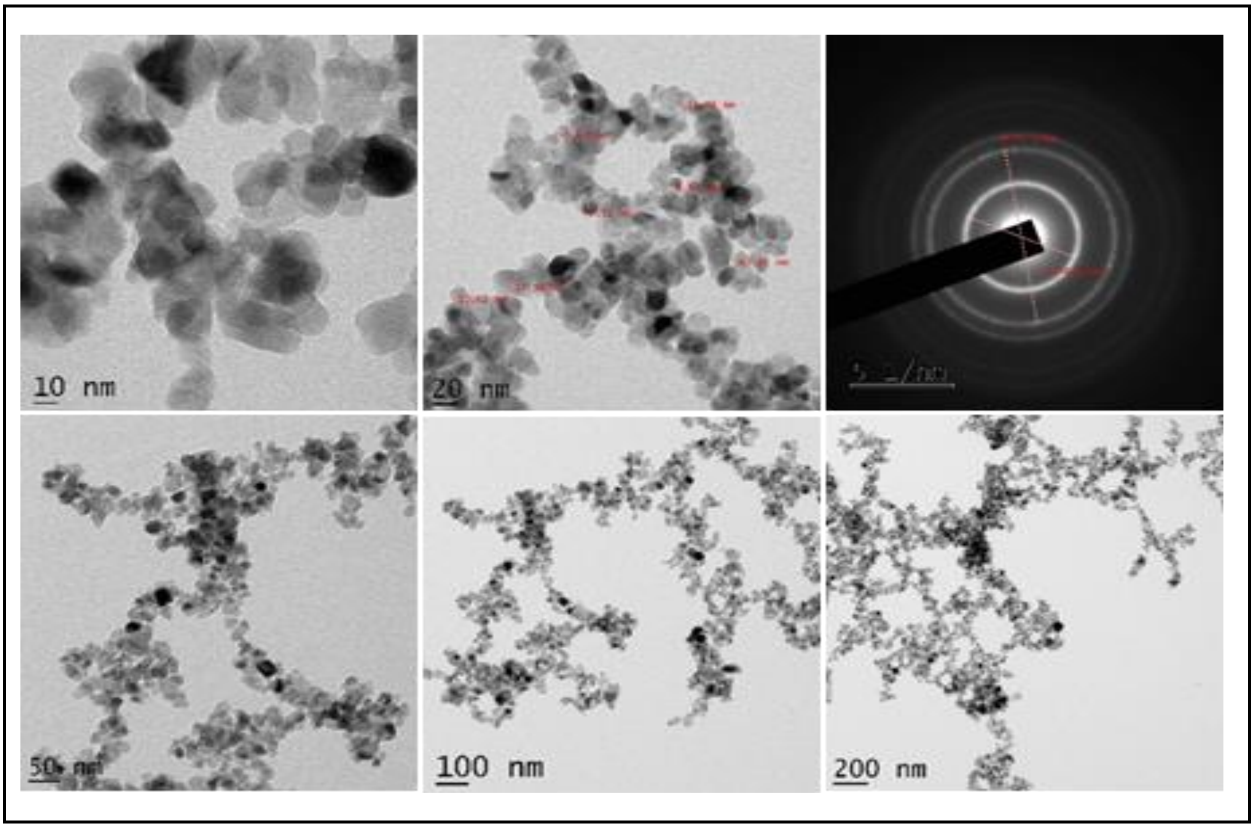

Fig. 5: TEM images of TiO2 and Ag-doped TiO2 nanocomposites.

For further confirmation of their growth pattern, to investigate precise particle size and the distribution of the crystallites, the Transmission electron microscopy (TEM) analysis has been done. Fig 5 illustrates the size and morphology of TiO_2: Ag NPs. The TEM images confirm the uniform size and spherical shape distribution of TiO_2: Ag is obtained at higher concentration of 10% of Ag with an average size of ~ 20 nm. The selected area diffraction (SEAD) pattern indicates spots attributed to the anatase TiO_2: Ag nanoparticles the measurement lattice fringes are characteristics for which the d-spacing corresponding to the rings are assigned respectively (Ruiz *et al.* 2004; Kalaiselvan *et al.* 2018), as shown in table 1.

3.3 FTIR spectroscopy of TiO_2: AgNPs

The Fourier transformed infrared spectroscopy (FTIR) of the synthesized TiO_2: Ag NPs have been shown in Fig. 6. The peaks are observed at 3425 and 2355, attributed to the Ti-OH bond (Blešić *et al.* 2002). The OH bending vibration of chemisorbed and/or physisorbed water molecule on the surface of the samples results in a relatively large band at ~1638 cm^{-1} for all the nanoparticles. The stretching vibrations of Ti-O-Ti bond (Blešić *et al.* 2002) are responsible for the powerful band in the 700-500 cm^{-1}range. The TiO_2: Ag nanoparticles FTIR spectra showed a peak of about 1200cm^{-1}, which was not seen in the undoped TiO_2. With the silver concentration in the synthesized samples, the intensity of this peak changed. The interaction between Ag and TiO_2 particles (Carotta *et al.* 1999) was tentatively assigned to the peak at 1200 cm^{-1}.

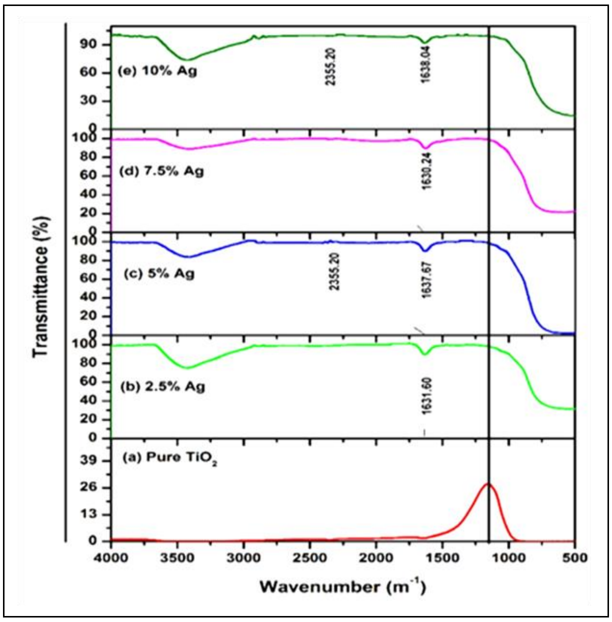

Fig. 6: FTIR of TiO_2 and Ag-doped TiO_2 nanocomposites.

3.4 PL spectrum of TiO_2: AgNPs

Photoluminescence spectroscopy has been carried out on the synthesized sample, the emission spectrum is observed at 383 nm, 450 nm, and 465 nm, respectively. The emission peaks appeared at higher wavelengths with respect to the band edge emission at 383 nm. These peaks are attributed to the quasi-free recombination at the absorption band edge, the shallow-trap state near the absorption band edge, the deep-trap band far below the band edge, and a combination of these effects are called the surface state emissions. The surface state emissions confirm the existence of Ag in TiO_2 NPs, and it increases with an increase in the concentration of Ag ions. Since, no capping agent has been used in this preparation, the quasi-free recombination and shallow trap emission overlap due to large size distribution. For trapped electrons and holes, the oxygen vacancies and surface hydroxyl groups are the most common locations. The visible photoluminescence in these nanoparticles is due to trapped carriers, which are absorbed by oxygen vacancies and surface hydroxyl groups. It is discovered that the emissions at 383 nm are excitonic emission. The emission peaks at 450 nm and 465 nm are related to the surface state emissions and are caused by trapped electron-hole resulting from dangling bonds in the TiO_2: Ag nanoparticles recombination. Hence, it can be concluded that the visible photoluminescence band appears due to the vacancy of oxygen associated with Ti^{3+} in anatase TiO_2 (Lee *et al.* 1999).

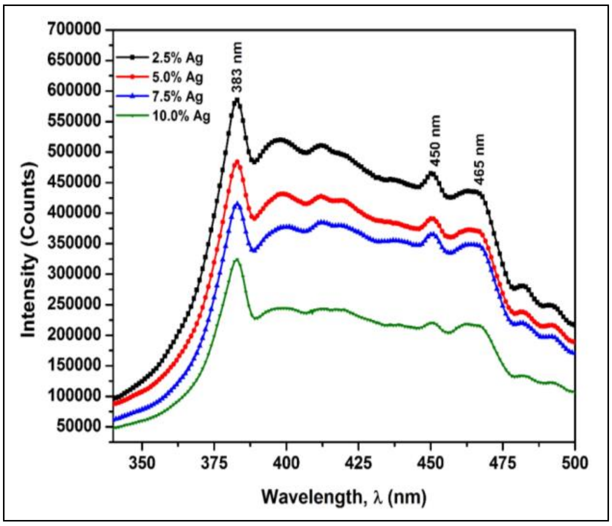

Fig 7: PL spectrum of TiO_2 and Ag-doped TiO_2 nanocomposites.

4. GAS SENSING PROPERTIES OF TiO_2:5% Ag NANOPARTICLES

Testing of the sample

Sensors were made by printing films of the nano-powders dispersed in water on (6 mm × 3 mm) ITO substrates with Au inter-digitated electrodes and an Au heater located on the backside. The sensors were placed inside a stainless-steel chamber to test the sensing properties. The electrical characterization has been carried out in a controlled atmosphere at room temperature, under synthetic dry air having a total stream of 100 sccm. The impedance data of the sensors has been collected in the two-point mode. Gases coming from certified bottles can be further diluted in the air at a given concentration by mass flow controllers. The sensor's sensitivity or response is given by (Sutka *et al.* 2012):

$$S = \frac{Z_a}{Z_g} \tag{2}$$

where Z_a is the resistance of sample measured at ambient environment while Z_g is resistance in the reference gas containing target gases. The gas concentration is calculated using the formula:

$$C_{ppm} = \frac{\delta \times V_r \times R \times T}{M \times P_b \times V_b} \times 10^6 \tag{3}$$

where δ is the density of ammonia solution, V_r is the volume of ammonia injected, T is the absolute temperature, R is the universal gas constant, M is the molecular weight and P_b and V_b are the pressure and volume of the chamber.

Fig. 8 illustrates the complex impedance plots (Nyquist or Cole-Cole plots) for 5 % Ag-doped TiO_2 sample with the operating temperature at 175 °C and different ammonia concentrations of 50 ppm, 250 ppm and 500 ppm, respectively. The sample shows only one semicircle, as evident from Fig 8. This is due to the progressive doping effect on crystallite size reduction. The number of grain boundaries increases as the size of the crystal shrinks, resulting in grain boundaries dominating only the conduction process (Samridhi *et al.* 2020). The nonlinear least square fitting routine was used to extract grain boundary parameters like resistance, capacitance, and relaxation time from impedance data. Fig. 8 shows that the semicircle of the sample shrinks as ammonia concentrations increase, which is due to the charge transfer to conduction.

Fig. 9 illustrates the discrepancy of imaginary impedance versus frequency of 5 % Ag-doped TiO_2 NPs at different ammonia concentrations. In the low-frequency region, the values are high; it could be due to the accumulation of free charges at the interface of pellet-electrolyte. All the curve points unite in the high-frequency region and then become independent of frequency, indicating the presence of relaxation in the system. The height of imaginary impedance is decreased as a function of temperature with the increase in ammonia concentrations.

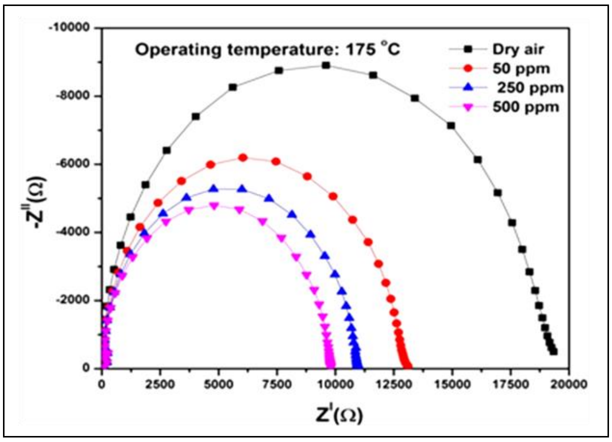

Fig. 8: The complex impedance spectrum of TiO_2:5%Ag nanoparticles.

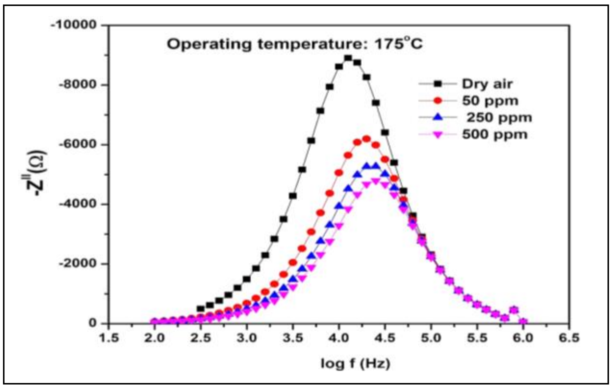

Fig. 9: Variation of the imaginary impedance of TiO_2:5%Ag NPs.

The sensitivity of the 5 % Ag-doped TiO_2 sensor has been calculated as a function of frequency using the above equation. Fig. 10 illustrates the variation of sensitivity with respect to frequency, exposed to 50 ppm, 250 ppm and 500 ppm ammonia. The maximum sensitivities obtained are 2.2, 3.1, 4.1 for 50, 250 and 500 ppm of ammonia, respectively.

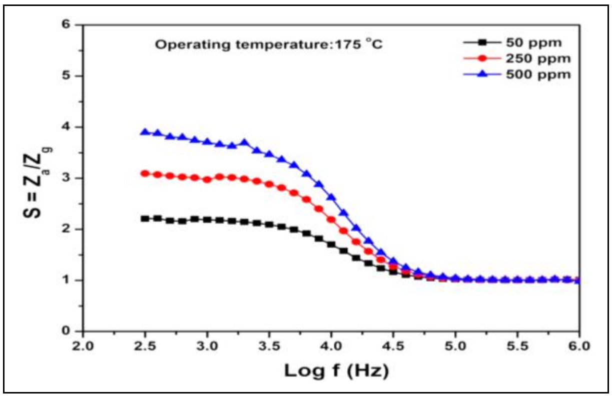

Fig. 10: Gas sensing properties of doped TiO_2:5%Ag nanoparticles.

5. CONCLUSION

Anatase phase TiO_2 and Ag: TiO_2 nanoparticles were synthesized by the Sol-gel method. Doping of Ag in TiO_2 suppresses the grain growth up to 5% then it was increased with increase of Ag concentration beyond 5 %. The TEM analysis reveals the formation of nano-sized TiO_2 particles. The EDS and FTIR confirm the presence of Ag, Ti and O. In PL spectra, the emissions at 383 nm, 450 nm and 465 nm confirm the presence of Ti, Ag and O. 5% Ag-doped TiO_2 shows the good response for NH_3 gas sensor application.

FUNDING

This research received no specific grant from any funding agency in the public, commercial, or not-for-profit sectors.

CONFLICTS OF INTEREST

The authors declare that there is no conflict of interest.

COPYRIGHT

REFERENCES

Ament, W., Huizenga, J., Kort, E., van der Mark, T., Grevink, R. and Verkerke, G., Respiratory ammonia output and blood ammonia concentration during incremental exercise, *Int. J. Sports Med.*, 20(2), 71–77 (1999).
https://dx.doi.org/10.1055/s-2007-971096

Balachandran, K., Mageswari, S. and Preethi, A., Photocatalytic decomposition of A549-lung cancer cancer cells by TiO_2 nanoparticles, *Mater. Today Proc.*, 37(2), 1071–1074 (2021).
https://dx.doi.org/10.1016/j.matpr.2020.06.297

Balachandran, K., Mariappan, R. and Vijayan, S., Photocatalytic Activity of PVA Modified TiO_2 Nanoparticles, *J. Environ. Nanotechnol.*, 7(1), 01–11 (2018).
https://dx.doi.org/10.13074/jent.2018.03.181295

Blešić, M. D., Šaponjić, Z. , Nedeljković, J. and Uskoković, D., TiO_2 films prepared by ultrasonic spray pyrolysis of nanosize precursor, *Mater. Lett.*, 54(4), 298–302 (2002).
https://dx.doi.org/10.1016/S0167-577X(01)00581-X

Borini, S., White, R., Wei, D., Astley, M., Haque, S., Spigone, E., Harris, N., Kivioja, J. and Ryhänen, T., Ultrafast graphene oxide humidity sensors, *ACS Nano.*, 7(12), 11166–11173 (2013).
https://dx.doi.org/10.1021/nn404889b

Carotta, M., Ferroni, M., Gnani, D., Guidi, V., Merli, M., Martinelli, G., Casale, M. and Notaro, M., Nanostructured pure and Nb-doped TiO_2 as thick film gas sensors for environmental monitoring, *Sens. Actuators B Chem.*, 58(1–3), 310–317 (1999).
https://dx.doi.org/10.1016/S0925-4005(99)00148-3

De la Hoz, R. E., Schlueter, D. P. and Rom, W. N., Chronic lung disease secondary to ammonia inhalation injury: A report on three cases, *Am. J. Ind. Med.*, 29(2), 209–214 (1996).
https://dx.doi.org/10.1002/(SICI)1097-0274(199602)29:2<209::AID-AJIM12>3.0.CO;2-7

Erisman, J., Instrument development and application in studies and monitoring of ambient ammonia, *Atmos. Environ.*, 35(11), 1913–1922 (2001).
https://dx.doi.org/10.1016/S1352-2310(00)00544-6

Gurlo, A., Nanosensors: Towards morphological control of gas sensing activity. SnO_2 , In_2O_3, ZnO and WO_3 case studies, *Nanoscale.*, 3(1), 154–165 (2011).
https://dx.doi.org/10.1039/C0NR00560F

Hossein-Babaei, F., Lajvardi, M. M. and Boroumand, F. A., Large area Ag–TiO_2 UV radiation sensor fabricated on a thermally oxidized titanium chip, *Sens. Actuators A Phys.*, 173(1), 116–121 (2012).
https://dx.doi.org/10.1016/j.sna.2011.10.028

Izu, N., Hagen, G., Schönauer, D., Röder-Roith, U. and Moos, R., Application of $V_2O_5/WO_3/TiO_2$ for Resistive-Type SO_2 Sensors, *Sensors.*, 11(3), 2982–2991 (2011).
https://dx.doi.org/10.3390/s110302982

Kalaiselvan, S., Balachandran, K., Karthikeyan, S. and Venckatesh, R., Botanical hydrocarbon sources based MWCNTs synthesized by spray pyrolysis method for DSSC applications, *Silicon.*, 10(2), 211–217 (2018).
https://dx.doi.org/10.1007/s12633-016-9419-7

Kalaivani, T. and Anilkumar, P., Role of Temperature on the phase modification of TiO_2 nanoparticles synthesized by the precipitation method, *Silicon.*, 10(4), 1679–1686 (2018a).
https://dx.doi.org/10.1007/s12633-017-9652-8

Kalaivani, T., AnilKumar, P., Synthesis of TiO_2:Ce nanoparticles for development of ammonia gas sensors, *J. Mater. Sci. Mater. Electron.*, 29(12), 9920–9929 (2018b).
https://dx.doi.org/10.1007/s10854-018-9034-z

Kılıç, Ç., Zunger, A., Origins of coexistence of conductivity and transparency in SnO_2, *Phys. Rev. Lett.*, 88(9), 095501 (2002).
https://dx.doi.org/10.1103/PhysRevLett.88.095501

Lee, D., Nitrogen oxides-sensing characteristics of WO_3-based nanocrystalline thick film gas sensor, *Sens. Actuators B Chem.*, 60(1), 57–63 (1999).
https://dx.doi.org/10.1016/S0925-4005(99)00244-0

Lehner, P., Staudinger, C., Borisov, S. M. and Klimant, I., Ultra-sensitive optical oxygen sensors for characterization of nearly anoxic systems, *Nat. Commun.*, 5(1), 4460 (2014).
https://dx.doi.org/10.1038/ncomms5460

Liu, X., Yang, J., Wang, L., Yang, X., Lu, L. and Wang, X., An improvement on sol-gel method for preparing ultrafine and crystallized titania powder, *Mater. Sci. Eng. A.*, 289(1–2), 241–245 (2000).
https://dx.doi.org/10.1016/S0921-5093(00)00901-1

McFarland, E. W. and Tang, J., A photovoltaic device structure based on internal electron emission, *Nature.*, 421(6923), 616–618 (2003).
https://dx.doi.org/10.1038/nature01316

Miura, N., Nakatou, M. and Zhuiykov, S., Impedancemetric gas sensor based on zirconia solid electrolyte and oxide sensing electrode for detecting total NO_x at high temperature, *Sens. Actuators B Chem.*, 93(1–3), 221–228 (2003).
https://dx.doi.org/10.1016/S0925-4005(03)00196-5

Pinder, R. W., Gilliland, A. B., Dennis, R. L., Environmental impact of atmospheric NH_3 emissions under present and future conditions in the eastern United States, *Geophys. Res. Lett.*, 35(12), n/a-n/a (2008).
https://dx.doi.org/10.1029/2008GL033732

Ruiz, A. M., Arbiol, J., Cornet, A., Shimanoe, K., Morante, J. R., Yamazoe, N., HRTEM/EELS Analysis, structural characterization and sensor performances of hydrothermal nano-TiO_2, *MRS Proc.*, 828, A4.10 (2004).
https://dx.doi.org/10.1557/PROC-828-A4.10

Samridhi, Singh, K. and Alvi, P. A., Influence of the pressure range on temperature coefficient of resistivity (TCR) for polysilicon piezoresistive MEMS pressure sensor, *Phys. Scr.*, 95(7), 075005 (2020).
https://dx.doi.org/10.1088/1402-4896/ab93e7

Sharma, M., Aljawfi, R. N., Kumari, K., Chae, K. H., Gautam, S., Dalela, S., Alvi, P. A., Kumar, S., Investigation of local atomic structure of Ni-doped SnO_2 thin films via X-ray absorption spectroscopy and their magnetic properties, *J. Mater. Sci. Mater. Electron.*, 30(1), 760–770 (2019a).
https://dx.doi.org/10.1007/s10854-018-0345-x

Sharma, M., Naji Aljawfi, R., Kumari, K., Chae, K. H., Dalela, S., Gautam, S., Alvi, P. A., Kumar, S., Investigation of local geometrical structure, electronic state and magnetic properties of PLD grown Ni-doped SnO_2 thin films, *J. Electron Spectros. Relat. Phenomena.*, 232, 21–28 (2019b).
https://dx.doi.org/10.1016/j.elspec.2019.01.002

Shi, L., Naik, A. J. T., Goodall, J. B. M., Tighe, C., Gruar, R., Binions, R., Parkin, I. and Darr, J., Highly Sensitive ZnO Nanorod- and Nanoprism-Based NO_2 Gas Sensors: Size and shape control using a Continuous Hydrothermal Pilot Plant, *Langmuir.*, 29(33), 10603–10609 (2013).
https://dx.doi.org/10.1021/la402339m

Sutka, A., Mezinskis, G., Lusis, A. and Jakovlevs, D., Influence of iron non-stoichiometry on spinel zinc ferrite gas sensing properties, *Sens. Actuators B Chem.*, 171–172, 204–209 (2012). https://dx.doi.org/10.1016/j.snb.2012.03.012

Tang, Y.-L., Li, Z.-J., Ma, J.-Y., Guo, Y.-J., Fu, Y.-Q. and Zu, X.-T., Ammonia gas sensors based on ZnO/SiO_2 bi-layer nanofilms on ST-cut quartz surface acoustic wave devices, *Sens. Actuators B Chem.*, 201, 114–121 (2014). https://dx.doi.org/10.1016/j.snb.2014.04.046

Wang, S.-Y., Ma, J.-Y., Li, Z.-J., Su, H. Q., Alkurd, N. R., Zhou, W.-L., Wang, L., Du, B., Tang, Y.-L., Ao, D.-Y., Zhang, S.-C., Yu, Q. K., Zu, X.-T., Surface acoustic wave ammonia sensor based on ZnO/SiO_2 composite film, *J. Hazard. Mater.*, 285, 368–374 (2015). https://dx.doi.org/10.1016/j.jhazmat.2014.12.014

Weppner, W., Solid-state electrochemical gas sensors, *Sens. Actuators.*, 12(2), 107–119 (1987). https://dx.doi.org/10.1016/0250-6874(87)85010-2

Yu'e, L. and Erda, L., Emissions of N_2O, NH_3 and NO_x from fuel combustion, industrial processes and the agricultural sectors in China, *Nutr. Cycl. Agroecosystems.*, 57(1), 99–106 (2000). https://dx.doi.org/10.1023/A:1009828705104